Microlattice Metamaterials for Tailoring Ultrasonic Transmission with Elastoacoustic Hybridization

Sebastian Krödel[1,†] and Chiara Daraio[2,*]

[1]*Department of Mechanical and Process Engineering,
Swiss Federal Institute of Technology (ETH), 8092 Zürich, Switzerland*
[2]*Engineering and Applied Science, California Institute of Technology, Pasadena, California 91125, USA*

Materials with designed microscale architectures, like microlattices, can achieve extreme mechanical properties. Most studies of microlattices focus on their quasistatic response, but their structural dimensions naturally prime them for ultrasonic applications. Here we report that microlattices constitute a class of acoustic metamaterials that exploit elastoacoustic hybridization to tailor ultrasonic wave propagation. Selecting the microlattice geometry allows the formation of hybridization band gaps that effectively attenuate (by >2 orders of magnitude) acoustic signals. The hybridization gaps stem from the interaction of pressure waves in a surrounding medium (e.g., water) with localized bending modes of the trusses in the microlattice. Outside these band gaps, the microlattices are highly transmissive (>80%) because their acoustic impedance is close to that of water. Our work can have important implications in the design of acoustic metamaterial applications in biomedical imaging, cell-based assay technology, and acoustic isolators in microelectromechanical systems.

I. INTRODUCTION

Microlattices are microscale periodic structures composed of slender trusslike elements arranged in different three-dimensional (3D) geometries. Structuring their geometry enables the creation of materials with extreme quasistatic [1–6] or multifunctional properties. For example, they are shown to present zero shear modulus [7,8], high strength and low density [1,2,9], negative Poisson ratio [10], and optomechanical effects [11]. Design approaches for static properties of microlattices mostly rely on (i) varying the lattice constitutive materials [1–3,5] and/or (ii) selecting the unit cell geometries [6,12]. Microlattice materials resemble perfectly ordered foams with tunable porosity and stiffness. Foams are commonly used as vibration- and sound-absorbing materials [13], and their properties are classically described by Biot's theory for low- and medium-frequency ranges [14,15]. For fluid-saturated foams, energy is carried both by pressure waves in the fluid and stress waves propagating in the elastic frame, and both fields are strongly coupled. The dominant dissipation mechanisms that are exploited for vibration or sound absorption and attenuation are viscoelastic and vibroacoustic effects in the solid frame and at the solid or fluid interface [13]. However, Biot's theory is only valid for low-frequency wave propagation, i.e., with wavelengths much larger than the pore size. Studying ordered microlattice architectures in a fluid medium, we show that at high frequency (i.e., with excitation wavelengths in the order of the pore size), coherent effects govern the propagation of acoustic energy.

Recent approaches to control the propagation of high-frequency ultrasound led to the development of soft acoustic metamaterials [16–19]. These materials exploit subwavelength resonators that are embedded in an acoustic host fluid [16,17,20,21]. Resonators can be formed from bubbles that show Minnaert resonances [20,21], low-density particles exploiting low-frequency acoustic Mie resonances [16], or thin films in liquid foams [19]. The study of metamaterials revealed acoustic properties desirable in acoustic applications [22,23]. For example, negative-refractive-index materials have been proposed to create lenses for subwavelength imaging [24–27], and acoustic rectification has been suggested to improve acoustic detection [28]. However, many metamaterials have been presented as proof-of-principle demonstrations on macroscopic scales [22,23,27] creating the need for microscale tailorable solutions that can function in the megahertz-frequency regime, of interest to biomedical applications.

Here, we propose and experimentally demonstrate a class of acoustic metamaterials formed by microlattices that exploit hybrid elastoacoustic resonances [Fig. 1(a)] and operate in the megahertz domain. We envision microlattice metamaterials that are immersed in a fluid and interact with propagative acoustic waves. To target water-based applications, we design polymeric microlattices with acoustic impedance matching that of water. This renders them

[*]Corresponding author.
daraio@caltech.edu
[†]skroedel@ethz.ch

acoustically transparent over large-frequency regions and allows for an effective coupling of acoustic and structural modes.

II. DESIGN OF MICROLATTICE METAMATERIALS

We use a diamondlike lattice symmetry [Fig. 1(a)] with a lattice constant of $a = 70 \, \mu$m as a model system because of its low effective density. One unit cell consists of four trusses that are connected to a joint. The lattice is created by the tessellation of individual unit cells along the lattice vectors $\mathbf{a}_1$, $\mathbf{a}_2$, and $\mathbf{a}_3$, which reflect the space symmetry of the periodic structure. The total length of a truss element is $L_0 = 30 \, \mu$m. To select the target frequency ranges of operation, we vary the geometry of the truss elements in the unit cell [Fig. 1(a)]. We assume a slightly elliptical member's cross section with an axis ratio of 1.4 to account for fabrication constraints (see Appendix A). To tailor the occurring hybridization modes, we propose a continuously varying cross section between the two radii R_0 and R_1 (see Appendix A). The radius R_0 is chosen to be always bigger than R_1. To control the final metamaterial properties, we exploit the first elastoacoustic bending mode of the truss elements [Fig. 1(b)].

We use finite-element analysis (COMSOL Multiphysics©) to calculate the first bending eigenfrequency f_0 for a truss immersed in water [Fig. 1(b)]. The frequency of the localized mode can be tuned by adjusting the parameters R_0 and R_1 [Fig. 1(b)]. The coupled mode creates a strong acoustic dipole [Fig. 1(b)]. For our analysis, we focus on two different kinds of lattices: The first one (lattice A) consists of tapered trusses with a varying radius between 6 and $1.5 \, \mu$m resulting in a relative lattice density of 7.5% [Fig. 1(c)–(e)]. For lattice A, we predict a highly localized coupled elastoacoustic resonance at 33 MHz. The second one (lattice B) is the simple case of a lattice with a constant cross section of $3.5 \, \mu$m and a relative lattice density of 6.4% [Fig. 1(f)]. Lattice B results in a first bending eigenfrequency of approximately 16 MHz. This lattice is chosen due to its relatively simple geometry, which can be readily fabricated using, for instance, interference self-propagating photopolymer waveguide lithography [29].

We fabricate 3D microlattice samples [Figs. 1(c)–1(f)] using a commercial 3D direct-laser-writing system (Nanoscribe™). The samples are written using a negative tone photoresist (IP-Dip™) on a fused silica substrate. The bulk modulus of polymerized IP-Dip is $E = 5.5$ GPa, as obtained from nanoindentation measurements in our lab (see Appendix B). The IP-Dip density is $\rho = 1100$ kg m^{-3} and its Poisson ratio is $\nu = 0.49$ [6]. We develop an algorithm that minimizes the laser's scanning path in the Nanoscribe tool to reduce the writing time and allow for the fabrication samples with an approximate $4 \times 4 \times 1$ mm^3 volume and an overall number of unit cells approximately
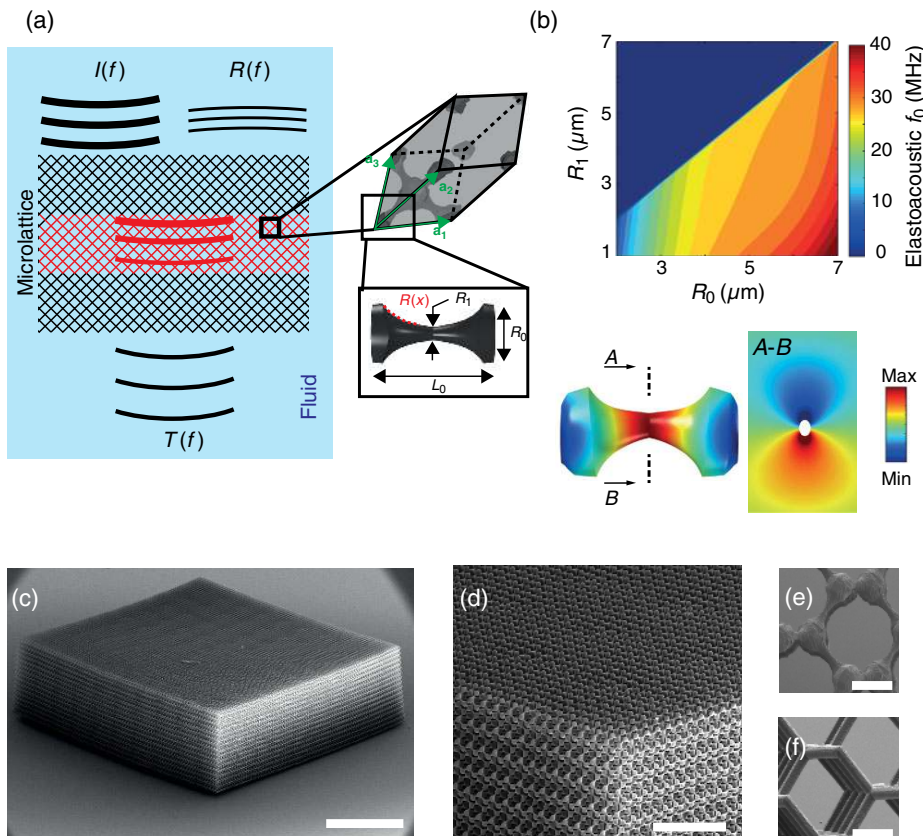

FIG. 1. (a) Working principle of the proposed microlattice. Incoming ultrasonic waves $I(f)$ hybridize with structural modes in the microlattice, which filter selective frequency components. This results in filtered transmitted $T(f)$ and reflected $R(f)$ ultrasonic signals. The microlattice properties are defined by its unit cell (with lattice vectors a_1, a_2, a_3) and by the truss elements (beams) geometry. (b) Frequency mapped as a function of geometry (top), displacement (bottom left), and acoustic dipole pressure distribution (bottom right) of the hybrid acoustic-elastic mode of a single-truss element. This mode is coupled to propagating pressure waves. (c) SEM image of a sample fabricated via two-photon lithography (scale bar is 1 mm). (d) Closer view showing the individual truss elements (scale bar is 200 μm). (e) Lattice A with tapered truss elements (scale bar is 20 μm). (f) Lattice B with constant cross-section truss elements (scale bar is 20 μm).
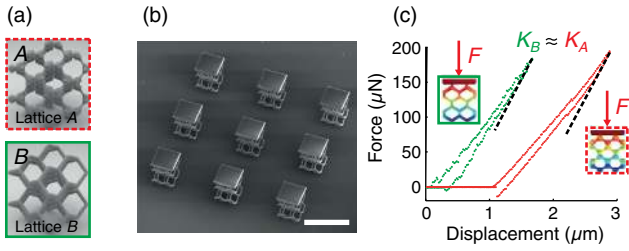
FIG. 2. (a) Parametrizations for lattices A and B. (b) SEM image of an array of lattice B specimens produced using the Nanoscribe system used for static experimental characterization (scale bar is 200 μm). (c) Results of the static compression tests for lattices A and B. Dashed lines represent the slope averaged over the first 0.25 μm of unloading. The red curve is shifted to ease visualization.

50×10^3. We begin our analysis investigating the quasistatic properties of the dry lattices. To experimentally test the lattices' quasistatic properties, we fabricate smaller compression test samples of lattice A, with a tapered cross section 6 to 1.5 μm, and lattice B with a constant cross section 3.5 μm [Fig. 2(a)].

The static compression experiments are performed using a microcompression sensor from FemtoTools™ (see Appendix B). To ensure a uniform compression of the microlattices, we fabricate a thick (10 μm) polymeric plate on top of the samples [Fig. 2(b)]. The stiffness of this plate is by design much larger than the effective stiffness of the lattices. The results of the static compression experiments for the two chosen parametrizations show a linear elastic response with small variations between loading and unloading [Fig. 2(c)]. We derive the effective stiffness of each lattice by taking the slope of the elastic unloading to avoid the presence of possible alignment issues during loading. In the investigated configuration, the measured stiffness of the two lattices is very similar (184 N/m in lattice B and 185 N/m in lattice A) despite the difference in the geometry of the truss elements. This is because the overall static stiffness of the lattices is influenced by the stiffness of the joints and the bending deformation of the trusses, which in our designs compensate each other. In lattice A, the joints are stiffer and the beams are more slender in the middle, so the static performance becomes comparable to lattice B, where the joints are softer but the beams do not bend as easily. We test many combinations of R_0 and R_1 and create a design map of the static properties for the studied lattice system (see Fig. S1 of the Supplemental Material [30]).

III. DISPERSION RELATIONS

Starting from the quasistatic measurements, we investigate the acoustic properties of the studied microlattice metamaterials when submersed in water. We numerically study the coupled acoustic or solid wave propagation in the thickness direction by deriving the microlattices' dispersion relations using COMSOL Multiphysics.

For lattice A, we derive the dispersion relations for two distinct cases: (i) an infinitely stiff solid [Fig. 3(a)] and (ii) an elastic solid [Fig. 3(b)]. The dispersion relations are obtained by applying Bloch boundary conditions on the faces of the unit cell [Figs. 3(a) and 3(b)] and solving the resulting eigenvalue problem for the eigenfrequencies with varying wave number k_z within the first Brillouin zone.

For the rigid structure (neglecting any elastic modes of the lattice), we observe only the first acoustic mode starting from the zero point. This mode shows nondispersive propagation up to the first zone folding, with a group and phase velocity close to the free propagation of plane waves in water. Afterwards, the plane-wave mode approaches a strongly coupled quasiplane mode and shows a first-level repulsion. At higher frequencies, around 40 MHz, another level repulsion yields the occurrence of a small, purely acoustic band gap.

The dispersion relation in the case of the elastic microlattice (including the coupling of structural and acoustic modes) shows a different response [Fig. 3(b)], which we analyze studying the pressure and displacement mode shapes at a distinct location in the dispersion diagram [Fig. 3(c)]. The resulting mode branches show highly
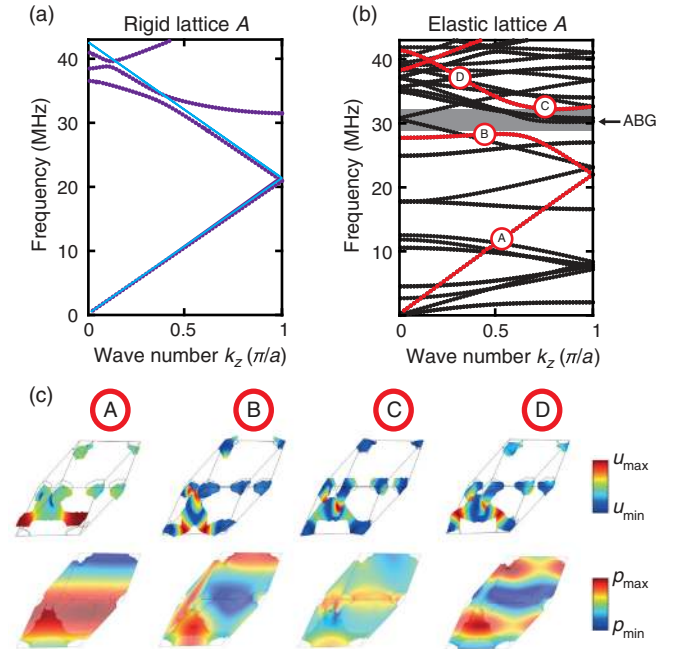

FIG. 3. (a) Dispersion relation for acoustic waves traveling in the z direction through a perfectly rigid lattice A (purple). The first plane pressure mode in pure water (blue line) is reported for comparison. (b) Dispersion relation for acoustic waves traveling in the z direction through an elastic lattice. The plane-wave mode is highlighted in red. We mark the position of the acoustic band gap (ABG). (c) Displacement and pressure fields before (part A) in the vicinity (parts B and C), and after (part D) the hybridization gap.

coupled pressure and displacement fields [Fig. 3(b)]. In this case, we observe four different modes starting from the zero point: a primarily acoustic mode (highlighted in red), a longitudinal mode of the lattice, and two degenerate shear modes of the lattice. We focus on the propagation of the first plane acoustic mode, as it is the only mode that can be excited by the ultrasonic transducers, due to its symmetry. Moreover, the first acoustic mode shows by far the highest group velocity of all occurring modes [Fig. 3(b)] and, therefore, dominates the energy transport in the water-saturated microlattice material.

The initial plane-wave mode propagates almost undistorted through the microlattice at low frequencies [Figs. 3(b) and 3(c) part A]. After the first band folding, the initially nondispersive mode hybridizes with the elastoacoustic bending mode of the trusses around 30 MHz to form a large band gap. The displacement and the pressure field at the edges of the hybridization band gap show the localized bending modes of the single truss elements and the corresponding pressure fields [Figs. 3(b) and 3(c) parts B and C]. The gap is bound by the in-phase mode of all four trusses [Fig. 3(c) part B] and the out-of phase mode of the lower and upper pair of trusses [Fig. 3(c) part C]. The two branches show a very low group velocity [Fig. 3(b)] throughout the first Brillouin zone. After the band gap, the plane-wave mode is recovered [Fig. 3(c) part D]. The hybridization band-gap frequency is slightly lower than the one predicted from the single-truss model [Fig. 1(b)]. This is due to the fixed-boundaries assumption used to calculate the response of the single truss, which assumes infinitely stiff joints. In the lattice itself, the beams are less constrained even though lattice A is constructed with rather stiff joints. We note that the same flat modes occur in the case of a dry lattice; however, they do not open a structural band gap (Fig. S2 of the Supplemental Material [30]).

We also analyze the wave propagation in the x direction showing the occurrence of an additional band gap due to the perpendicular motion of the beams (i.e., beams bending in the x-y plane; Fig. S3 of the Supplemental Material [30]) highlighting that the occurrence of band gaps can be direction dependent. For the rest of the discussions, we focus on propagation in the z direction because this direction is also tested experimentally.

We study the acoustic properties of lattice B by deriving the dispersion relations for both a perfectly rigid [Fig. 4(a)] and an elastic solid [Fig. 4(b)]. For the rigid structure, we observe similar dispersion characteristics as in lattice A [Fig. 3(a)], with slightly less repelling modes. The dispersion relation for the elastic lattice B is shown in Fig. 4(b). In contrast to lattice A [Fig. 3(b)], we observe two hybridization band gaps in the investigated frequency region. The first one occurs around 15.2 MHz and is caused by the coupling of the plane mode to the first bending mode of the lattice truss element [see inset of Fig. 4(b)], as predicted by the study of one single truss [Fig. 1(b)].
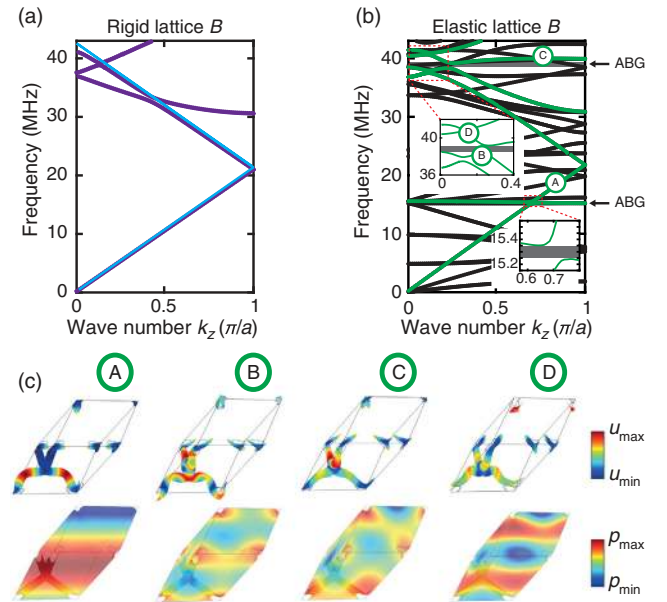

FIG. 4. (a) Dispersion relation for acoustic waves traveling in the z direction through a perfectly rigid lattice B (purple). The first plane pressure mode in pure water (blue line) is reported for comparison. (b) Dispersion relation for acoustic waves traveling in the z direction through an elastic lattice B. The plane-wave mode is highlighted in green. We mark the position of the acoustic band gaps (ABG). (c) Displacement and pressure fields before (part A), in the vicinity (parts B and C), and after (part D) the second hybridization gap.

The width of the band gaps is significantly smaller than the one triggered by the first bending mode in lattice A. This is due to the fact that the joints in lattice B are soft and lead to a higher coupling between neighboring beams, which prevents an effective localization of the mode.

At higher frequencies, we find another larger band gap caused by the hybridization with the second bending eigenmode of the truss elements [see the inset in Fig. 4(b)]. To analyze the features of coupled wave propagation in the vicinity of the second band gap, we analyze the pressure and displacement fields [Fig. 4(c)]. The initial plane acoustic pressure mode [Fig. 4(c) part A] becomes highly localized and asymmetric at the lower and upper edge of the second occurring band gap [Fig. 4(c) parts B and C]. The displacement fields at the band-edge frequencies are again dominated by bending modes of the trusses. At higher frequencies, the initial plane-wave mode is recovered [Fig. 4(c) part A], and we observe the second-level repulsion as in the rigid lattice case [Fig. 4(a)].

IV. TRANSMISSION PROPERTIES

To test the wave-propagation properties within the lattices experimentally, we build a customized water tank for ultrasonic testing (see Appendix B) similar to the one described in Ref. [31]. The fabricated microlattices are glued to an acrylic glass frame, to allow their

characterization freestanding (i.e., without the influence of a substrate). We excite a frequency chirp in the range between 12 and 45 MHz with wavelengths between 125 and 33 μm in water, respectively (see Appendix B). The wavelengths (λ) are larger than the characteristic lengths of the truss elements ($L_0 < \lambda$ and R_0, $R_1 \ll \lambda$). We show the ultrasonic pulses transmitted through the microlattice samples A and B and pure water measured experimentally in Fig. 5(a). For both lattice samples, we observe a frequency-dependent effect on the transmitted signal [Fig. 5(a)]. The microlattices affect the transmission of the chirps mostly at higher frequencies, as expected from the numerical results [Figs. 3(b) and 4(b)]. Experimental transmission curves are then obtained from analyzing the frequency spectrum of the transmitted waveforms. We calculate the transmission for the microlattice relative to the transmitted pressure field in pure water [Figs. 5(b) and 5(c)].

For lattice A, the maximum attenuation is reached at approximately 30 MHz. The size and position of the observed transmission dip shows a good agreement with the numerical band-gap position [Fig. 3(b)]. The broadening of the attenuation zone can be due to uncertainties in the geometry of the fabricated samples and to viscous effects that become important at the microscale [32]. In particular, the inner diameter ($R_1 = 1.5$ μm) of the members of lattice A is close to the minimum feature size of the direct-laser-writing tool. When fabricating samples close to the resolution limit of the tool, we find variability on the resulting radii with features erring towards slightly larger radii. These fabrication errors lead to the broadening of the band gap towards lower frequencies. This trend is in

line with the simulations performed for the single-truss elements [Fig. 1(b)]. The experimental decrease in transmission within the band gap for lattice A is approximately 2 orders of magnitude.

For lattice B, the size and position of the occurring dips in transmission agree equally well with the prediction from the dispersion relation [Fig. 4(b)]. Besides the large dip in transmission around 37 MHz induced by the second bending eigenmode and a maximum attenuation of 1 order of magnitude, both the experiment results and the numerical model [Fig. 4(b)] show a small dip in transmission due to the hybridization mode at 15.2 MHz [see inset of Fig. 5(c)].

We note that the microlattices are also highly transparent to incoming acoustic waves over large-frequency regions due to their acoustic impedance matched with water, with a transmission of more than 80% up to 25 MHz [Figs. 5(b) and 5(c)].

We perform fully 3D frequency domain finite-element simulations of the rigid and elastic lattices A and B with a total thickness of approximately $L_b = 300$ μm, about 3 times smaller than the experimental samples [Figs. 5(b) and 5(c)]. Plane harmonic pressure waves with an amplitude p_0 are excited on one side of the lattice, and the transmitted pressure $p_1(\omega)$ is obtained in the far field of the sample for lattice A [Fig. 6(a)]. At both the beginning and end of the domain, we add a perfectly matched layer to avoid reflections from the boundary. To account for an infinite extension in x and y, we add periodic boundary conditions to the sides of the domain. We also add an isotropic structural loss factor of $\eta = 0.025$ to the lattice material to account for dissipation in the polymer [33].
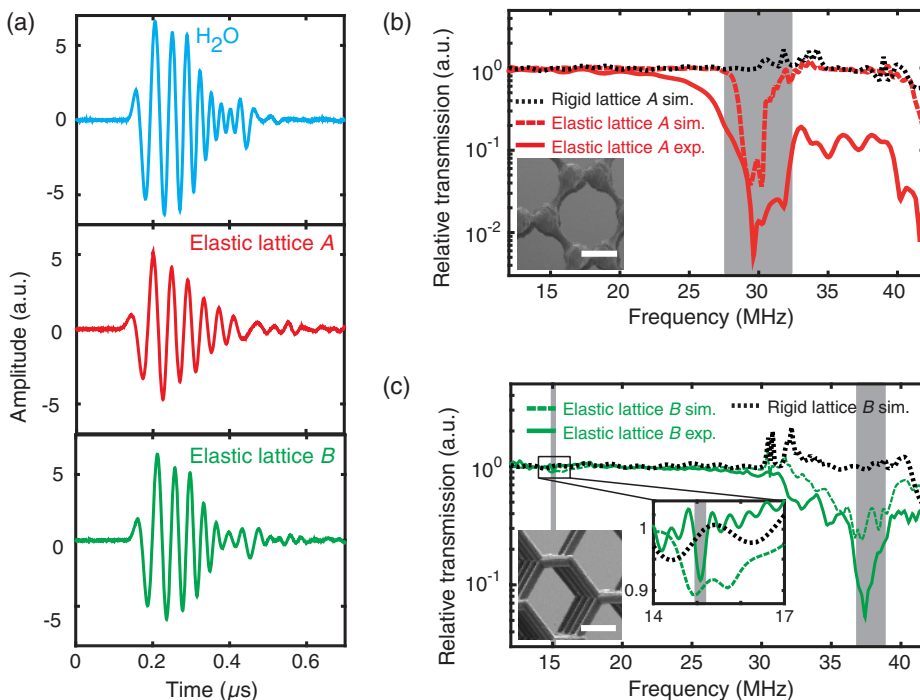

FIG. 5.   (a) Experimental ultrasonic waveforms for chirp signal between 15 and 45 MHz transmitted through water and the microlattices A and B. (b) Experimental and numerical transmission curves for the rigid and elastic microlattice A. The predicted band gap from the dispersion diagram in Fig. 3(b) is highlighted in gray (the scale bar in the SEM image on the inset is 20 μm). (c) Experimental and numerical transmission curves for the rigid and the elastic microlattice B. The predicted band gap from the dispersion diagram in Fig. 4(b) is highlighted in gray (the scale bar in the SEM image on the inset is 20 μm). The inset shows the first hybridization gap.
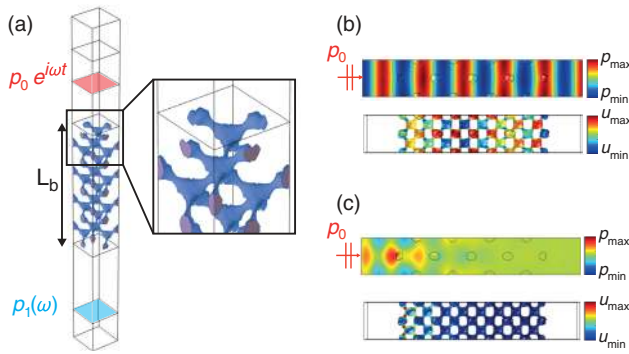
FIG. 6. (a) Numerical 3D model for finite-size transmission simulations using the cubic and not the primitive unit cell. (b) Side view of the numerical simulation of the pressure field and structural modes in the lattice *A* at 20 MHz (outside band gap). (c) Side view of the numerical simulation of the pressure field and structural modes in the lattice *A* at 30 MHz (inside band gap).

The numerical transmission results show that rigid lattices *A* and *B* do not present attenuation in the investigated frequency range [Figs. 5(b) and 5(c)]. The spectrum calculated for elastic lattices agrees well with the experimental results [Figs. 5(b) and 5(c)]. However, the numerical data show about 1 order of magnitude smaller attenuation compared to the one obtained experimentally due to the smaller sample thickness used in the computations. Larger sample thicknesses similar to the experimental samples (approximately 1 mm) cannot be simulated over the full frequency range due to the large number of degrees of freedom required in the finite-element model. To obtain a better quantitative comparison between the experiments and the simulations, we perform a single-frequency simulation with a full-size sample of lattice *A* ($3 \times L_b$) and find a transmission coefficient of $T = 1.1 \times 10^{-2}$ at 30 MHz. This is in good agreement with the experimental results, demonstrating the sample-size effect on attenuation.

Additionally, we analyze the pressure and displacement fields in the finite-size sample of lattice *A* before [Fig. 6(b)] and inside the band gap [Fig. 6(c)]. Incident plane waves at 20 MHz pass through the microlattice almost undistorted [Fig. 6(b)], while waves at 30 MHz decay rapidly along the sample's thickness [Fig. 6(c)]. Inside the band gap, we observe a strong localization of acoustic pressure and displacement fields and an overall reflection of the acoustic energy.

V. MICROLATTICE METAMATERIALS 2D SCANS

To demonstrate the dramatic change in transmissibility achievable by the microlattices, we perform experimental 2D scans in water of the pressure field below the samples when excited by a fixed-frequency signal. A top view of the lattice sample fixed in the acrylic glass frame serves as a reference image [Fig. 7(a)]. We investigate the transmission
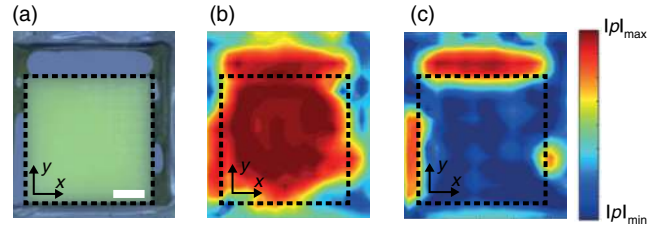

FIG. 7. (a) Top view of microlattice *A* glued to an acrylic glass frame (the scale bar is 2 mm). The black dashed line represents the sample edges. (b) Experimental transmission map of pressure waves in water transmitting through microlattice *A* at 20 MHz. (c) Experimental transmission map of pressure waves transmitting through microlattice *A* at 30 MHz.

at two representative frequencies: one in the propagation regime at 20 MHz [Fig. 7(b)] and one inside the band gap at 30 MHz [Fig. 7(c)]. Outside the band gap, the propagation remains plane and not attenuated [Fig. 7(b)], while within the band gap, the transmission is effectively blocked [Fig. 7(c)]. The pressure amplitudes in our experiments are between 10^{-2} and 10^{-1} MPa. We estimate the maximum sustainable pressure amplitudes before failure of the lattices to be around 5 MPa based on dry compression failure tests [5].

VI. CONCLUSION

The microlattices presented in this paper use elastoacoustic resonances to tailor the transmission and attenuation of ultrasonic pulses traveling through water. Using truss elements as a building block for the lattice design, we tailor the size and frequency position of their transmission band gaps independent of the static microlattice properties. Similar hybridization mechanisms can be exploited to design the dispersion of acoustic waves in other structured media, e.g., to create negative index metamaterials for subwavelength imaging. Their properties pave the way to the fabrication of acoustic devices based on resonant metamaterials.

The high transmissibility of ultrasonic signals with frequencies outside the band gaps makes microlattices advantageous in applications, where low reflectivity and narrow working frequencies are necessary. In this context, the targeted high-frequency range (approximately 30 MHz) renders them especially interesting for biomedical imaging applications that require high resolution and small penetration depths, such as imaging of the skin [34] or high-resolution imaging of vascular systems [35]. The proposed structures are completely scalable and can also be adapted to respond at lower frequencies that are closer to typical human ultrasonic imaging applications (approximately 1 MHz).

It is possible to envision the use of microlattice metamaterials for the design of ultrasonic transducers: By virtue of Rayleigh's principle of acoustics, the truss elements

are expected to be able to effectively convert incoming ultrasound waves into structural vibrations and vice versa. A possible excitation mechanism can be envisioned by doping the materials with piezoelectric nanoparticles [36] or carbon nanotubes [37] to allow for electrical or optical [38] excitation. As the pore size in the designed lattice materials corresponds to a typical biological cell size (10–100 μm), our metamaterial microlattices can find applications in technologies for cell-based assays, cell surgery, and cellular-scale microbalances. For biomedical applications using high-intensity ultrasound [38,39] (e.g., in targeted-cell therapy), higher dynamic pressure ranges are required. In order to withstand high amplitudes, the strength of the microlattices can be enhanced using stiffer materials [5,40].

The microlattices' small and adaptable size is also beneficial in MEMS devices [41], where they can find use as 3D isolators for thin-film resonators [42]. In these cases, the working frequencies of the microlattices can increase by decreasing the structural dimension [4] or using more rigid base materials [40].

APPENDIX A: LATTICE FABRICATION

We fabricate our lattice structures using the commercial Nanoscribe 3D direct laser writer. The geometries are initially created using the computer-aided-design (CAD) functionalities of COMSOL Multiphysics and then exported as stereolithography files. These files are further processed in Describe$^{©}$. Here the geometries are sliced into layers of 0.5 μm thickness. Each layer is hatched with lines with a distance of 0.35 μm. The difference in slicing and hatching is due to the voxel geometry, which is elliptical with an aspect ratio of 3.5 between height and width. Because of this geometry, the radii of the printed geometries are also slightly different from the CAD geometries and show elliptical instead of circular cross sections. The evolution between the two radii along the axis of the truss member is described by $R(x) = R_0(1 + \alpha x + \beta x^2)^{-1}$. We adapt the parameters α, β such that $R_{(L0/2)} = R_1$ and $R_{(L0/4)} = R_1 + 0.2 \times (R_0 - R_1)$. We perform SEM measurements to inform the numerical simulations with the actual geometry of the samples. To create large arrays of lattices, we optimize the standard input files prepared by Describe. This is done by sequentially writing the lines that are closest to each other. We use the galvoscanning mode of the machine with a scan speed of 50 mm/s. To create large samples ($4 \times 4 \times 1$ mm^3), we stitch together $400 \times 400 \times 70$ μm^3 lattices with a small overlap. To reach the heights of approximately 1 mm, the objective stage is moved in addition to the piezoelectric stages of the tool. The structures are written in the negative tone resist IP-Dip. After structuring, we develop the samples for 30 min in propylene-glycol-monomethyl-ether-acetate and 10 min in isopropanol.

APPENDIX B: EXPERIMENTAL METHODS

1. Nanoindentation tests

Nanoindentation tests were performed using a Hysitron TI Premier Nanoindenter. We produce 50-μm-thick circular plates with a radius of 400 μm with Nanoscribe using the same writing parameters as for the microlattices. We carry out indents with a 6-μm spherical tip under quasistatic conditions. The Young's module of the polymer is obtained by averaging over several locations on the sample.

2. Microcompression tests

Static compression tests are performed with a micro-compression sensor from FemtoTools. We use the FTL 1000 lateral force sensor with a flat tip of 50×50 μm^2. Prior to the actual structure, we perform a reference measurement on the glass substrate to obtain the stiffness of the experimental setup, which is used for further calculations of the lattice structural spring stiffness. For repeatability, we test 16 lattices of each type and average their stiffness. We perform load-controlled tests up to a maximum load of 200 μN at a strain rate of 0.1 μm/s. The plastic deformation due to the performed loading is negligible, which is shown by cyclic repetition (over five cycles) of the experiments.

3. Ultrasonic tests

The experimental setup consists of three main components: (i) a broadband nonfocused ultrasonic transducer (V356-SU, 30 MHz, Panametrics) to generate the acoustic excitation; (ii) a needle hydrophone (0.2-mm needle, Precision Acoustics) to measure the pressure in the far field; (iii) the sample and sample holder positioned between the transducer and the needle sensor. To avoid averaging errors, the effective measurement area of the hydrophone is much smaller than the size of the microlattices. To completely wet the polymeric microlattices in water, we flush the lattice with isopropanol before immersion. We drive the ultrasonic transducer with frequency chirps using a high-frequency lock-In amplifier (UHFLI, Zurich Instruments) connected to a 50-dB radio-frequency amplifier (325 LA, E&I). The 200-μm hydrophone is connected

to a signal conditioner, and the voltage signal is connected to the input port of the lock-in amplifier. The setup allows the collection of a low noise signal. The data analysis and instrument control are done in MATLAB$^{©}$. The ultrasonic tests are carried out in the beam maximum of the ultrasonic transducer. To find the maximum, the hydrophone is mounted on three-axis scanning stage, and frequency sweeps are performed on different locations until the maximum pressure amplitude is found. The ultrasonic beam is typically stable over 3–5 mm within the center. Once the maximum is found, the lattice sample is placed in between the transducer and the hydrophone. The hydrophone (0.2-mm needle, Precision Acoustics) shows a typical sensitivity of 50 nV/Pa in the considered frequency range. We use deionized water at room temperature and allow the hydrophone to rest in the water 30 min prior to the performed measurements. Two-dimensional scans are performed using a fine grid of points (distance 0.5 mm) in the x-y plane at the same z distance as used in the transmission experiment.

———————

[1] T. A. Schaedler, A. J. Jacobsen, A. Torrents, A. E. Sorensen, J. Lian, J. R. Greer, L. Valdevit, and W. B. Carter, Ultralight metallic microlattice, Science **334**, 962 (2011).

[2] L. R. Meza, S. Das, and J. R. Greer, Strong, lightweight and recoverable three-dimensional ceramic nanolattices, Science **345**, 1322 (2014).

[3] D. Jang, L. R. Meza, F. Greer, and J. R. Greer, Fabrication and deformation of three-dimensional hollow ceramic nanostructures, Nat. Mater. **12**, 893 (2013).

[4] J. Bauer, A. Schroer, R. Schwaiger, and O. Kraft, Approaching theoretical strength in glassy carbon nanolattices, Nat. Mater. **15**, 438 (2016).

[5] J. Bauer, S. Hengsbach, I. Tesari, R. Schwaiger, and O. Kraft, High-strength cellular ceramic composites with 3D microarchitecture, Proc. Natl. Acad. Sci. U.S.A. **111**, 2453 (2014).

[6] L. R. Meza, A. J. Zelhofer, N. Clarke, A. J. Mateos, D. M. Kochmann, and J. R. Greer, Resilient 3D hierarchical architected metamaterials, Proc. Natl. Acad. Sci. U.S.A. **112**, 11502 (2015).

[7] M. Kadic, T. Bückmann, N. Stenger, M. Thiel, and M. Wegener, On the practicability of pentamode mechanical metamaterials, Appl. Phys. Lett. **100**, 191901 (2012).

[8] T. Bückmann, M. Thiel, M. Kadic, R. Schittny, and M. Wegener, An elasto-mechanical unfeelability cloak made of pentamode metamaterials, Nat. Commun. **5**, 4130 (2014).

[9] X. Zheng, H. Lee, T. H. Weisgraber, M. Shusteff, J. Den Otte, E. B. Duoss, J. D. Kuntz, M. M. Biener, Q. Ge, J. A. Jackson, S. O. Kucheyev, N. X. Fang, and C. M. Spadaccini, Ultralight, ultrastiff mechanical metamaterials, Science **344**, 1373 (2014).

[10] T. Bückmann, N. Stenger, M. Kadic, J. Kaschke, A. Frölich, T. Kennerknecht, C. Eberl, M. Thiel, and M. Wegener, Tailored 3D mechanical metamaterials made by dip-in direct-laser-writing optical lithography, Adv. Mater. **24**, 2710 (2012).

[11] V. F. Chernow, H. Alaeian, J. A. Dionne, and J. R. Greer, Polymer lattices as mechanically tunable 3-dimensional photonic crystals operating in the infrared, Appl. Phys. Lett. **107**, 101905 (2015).

[12] M. F. Ashby, The properties of foams and lattices, Phil. Trans. R. Soc. A **364**, 15 (2006).

[13] P. Göransson, Acoustic, and vibrational damping in porous solids, Phil. Trans. R. Soc. A **364**, 89 (2006).

[14] M. A. Biot, Theory of propagation of elastic waves in a fluid-saturated porous solid. I. Low-frequency range, J. Acoust. Soc. Am. **28**, 168 (1956).

[15] M. A. Biot, Theory of propagation of elastic waves in a fluid-saturated porous solid. II. Higher frequency range J. Acoust. Soc. Am. **28**, 179 (1956).

[16] T. Brunet, A. Merlin, B. Mascaro, K. Zimny, J. Leng, O. Poncelet, C. Aristegui, and O. Mondain-Monval, Soft 3D acoustic metamaterial with negative index, Nat. Mater. **14**, 384 (2014).

[17] T. Brunet, J. Leng, and O. Mondain-Monval, Soft acoustic metamaterials, Science **342**, 323 (2013).

[18] Y. Lai, Y. Wu, P. Sheng, and Z.-Q. Zhang, Hybrid elastic solids, Nat. Mater. **10**, 620 (2011).

[19] J. Pierre, B. Dollet, and V. Leroy, Resonant Acoustic Propagation and Negative Density in Liquid Foams, Phys. Rev. Lett. **112**, 148307 (2014).

[20] T. Brunet, S. Raffy, B. Mascaro, J. Leng, R. Wunenburger, O. Mondain-Monval, O. Poncelet, and C. Aristegui, Sharp acoustic multipolar-resonances in highly monodisperse emulsions, Appl. Phys. Lett. **101**, 011913 (2012).

[21] V. Leroy, A. Strybulevych, M. Lanoy, F. Lemoult, A. Tourin, and J. H. Page, Superabsorption of acoustic waves with bubble metascreens, Phys. Rev. B **91**, 020301(R) (2015).

[22] S. A. Cummer, J. Christensen, and A. Alù, Controlling sound with acoustic metamaterials, Nat. Rev. Mater. **1**, 16001 (2016).

[23] G. Ma and P. Sheng, Acoustic metamaterials: From local resonances to broad horizons, Sci. Adv. **2**, e1501595 (2016).

[24] M. Kadic, T. Bückmann, R. Schittny, and M. Wegener, Metamaterials beyond electromagnetism, Rep. Prog. Phys. **76**, 126501 (2013).

[25] Y. Ding, Z. Liu, C. Qiu, and J. Shi, Metamaterial with Simultaneously Negative Bulk Modulus and Mass Density, Phys. Rev. Lett. **99**, 2 (2007).

[26] A. Sukhovich, L. Jing, and J. H. Page, Negative refraction and focusing of ultrasound in two-dimensional phononic crystals, Phys. Rev. B **77**, 014301 (2008).

[27] N. Kaina, F. Lemoult, M. Fink, and G. Lerosey, Negative refractive index and acoustic superlens from multiple scattering in single negative metamaterials, Nature (London) **525**, 77 (2015).

[28] B. Liang, X. S. Guo, J. Tu, D. Zhang, and J. C. Cheng, An acoustic rectifier, Nat. Mater. **9**, 989 (2010).

[29] A. J. Jacobsen, W. Barvosa-Carter, and S. Nutt, Micro-scale truss structures formed from self-propagating photopolymer waveguides, Adv. Mater. **19**, 3892 (2007).

[30] See Supplemental Material at http://link.aps.org/supplemental/10.1103/PhysRevApplied.6.064005 for static properties, design maps, dispersion relation of dry lattices,

and dispersion relation in the perpendicular propagation direction.

[31] S. Yang, J. Page, Z. Liu, M. Cowan, C. Chan, and P. Sheng, Ultrasound Tunneling through 3D Phononic Crystals, Phys. Rev. Lett. **88**, 104301 (2002).

[32] M. Molerón, M. Serra-Garcia, and C. Daraio, Visco-thermal effects in acoustic metamaterials: From total transmission to total reflection and high absorption, New J. Phys. **18**, 033003 (2016).

[33] M. F. Ashby, Materials Selection in Mechanical Design (Butterworth-Heinemann, Oxford, 2005).

[34] G. R. Lockwood, D. H. Turnbull, D. A. Christopher, and F. S. Foster, Beyond 30 MHz-Applications of high-frequency ultrasound imaging, IEEE Eng. Med. Biol. Mag. **15**, 60 (1996).

[35] C. Errico, J. Pierre, S. Pezet, Y. Desailly, Z. Lenkei, O. Couture, and M. Tanter, Ultrafast ultrasound localization microscopy for deep super-resolution vascular imaging, Nature (London) **527**, 499 (2015).

[36] A. Marino, J. Barsotti, G. De Vito, C. Filippeschi, B. Mazzolai, V. Piazza, M. Labardi, V. Mattoli, and G. Ciofani, Two-photon lithography of 3D nanocomposite piezoelectric scaffolds for cell stimulation, ACS Appl. Mater. Interfaces **7**, 25574 (2015).

[37] W. Xiong, Y. Liu, L. J. Jiang, Y. S. Zhou, D. W. Li, L. Jiang, J. F. Silvain, and Y. F. Lu, Laser-directed assembly of aligned carbon nanotubes in three dimensions for multifunctional device fabrication, Adv. Mater. **28**, 2002 (2016).

[38] H. W. Baac, J. G. Ok, A. Maxwell, K.-T. Lee, Y.-C. Chen, A. J. Hart, Z. Xu, E. Yoon, and L. J. Guo, Carbon-nanotube optoacoustic lens for focused ultrasound generation and high-precision targeted therapy, Sci. Rep. **2**, 989 (2012).

[39] J. E. Kennedy, High-intensity focused ultrasound in the treatment of solid tumours, Nat. Rev. Cancer **5**, 321 (2005).

[40] X. Wendy Gu and J. R. Greer, Ultra-strong architected Cu meso-lattices, Extr. Mech. Lett. **2**, 7 (2015).

[41] R. H. Olsson and I. El-Kady, Microfabricated phononic crystal devices and applications, Meas. Sci. Technol. **20**, 012002 (2009).

[42] K. M. Lakin, Thin film resonator technology, IEEE Trans. Ultrason. Ferroelectr. Freq. Control **52**, 707 (2005).